# Nanotwinned Copper Foil for "Zero Excess" Lithium−Metal Batteries

Chun-Cheng Lin, Zhen Chen, Holger Euchner, Tobias Eisenmann, Katrin Geng, Thomas Diemant, Shan Fang, Chih-Han Yen, Stefano Passerini,* Chi-Chang Hu,* and Dominic Bresser*

ABSTRACT: The "zero excess" lithium−metal battery cell concept, in which the pristine negative electrode consists only of the current collector, while all lithium is present only in the positive electrode active material, promises substantial improvements in energy density. However, the achievement of stable cycling for more than just a few cycles requires a careful design and adjustment of all cell components—especially the current collector at the negative electrode. Herein, we provide a comparative investigation of commercial, polycrystalline copper foil, characterized by a

rather random [111], [200], and [220] orientation and a high concentration of grain boundaries, and nanotwinned copper foil, which has a solely [111]-oriented grain structure. Remarkably, the plated lithium on the foil with [111] orientation reveals a much more homogeneous morphology independent of the current density applied, while several dendritic lithium deposits are observed on the polycrystalline copper foil. This also translates into higher Coulombic efficiency and stabilized cycling performance of Cu[111]∥ NMC_{811} cells, highlighting the important impact of the crystal orientation of the current collector.

KEYWORDS: nanotwinned copper, current collector, zero excess, lithium metal, negative electrode, NMC_{811}, battery
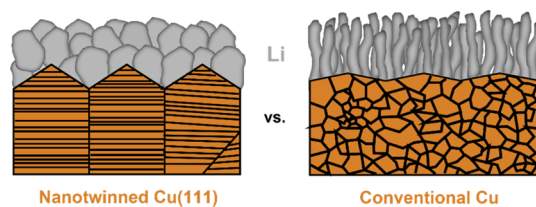
1. INTRODUCTION

The continuously increasing electrification of the transportation sector[1,2] and demand for batteries with greater energy density have revitalized the interest in lithium−metal batteries.[3−5] In such systems, the negative electrode commonly consists of a lithium metal foil on a metallic current collector (frequently copper foil), while the positive electrode active material is, for instance, $LiNi_{1−x−y}Mn_xCo_yO_2$. Accordingly, both electrodes provide lithium, and the cell contains a substantial—sometimes very large—excess of lithium, which prolongs the cycle life despite Coulombic efficiencies (CEs) being (significantly) lower than 100%.[6] However, this adds cost and renders the cell assembly more challenging owing to the high sensitivity of metallic lithium to an ambient atmosphere.[5,7,8] Not least, these considerations have triggered the rapidly rising interest in so-called "anode-free" or "zero excess" lithium−metal batteries, in which the positive electrode is the only source of lithium. The negative electrode consists of the appropriately modified current collector only, serving as a substrate for the deposition of metallic lithium upon charging the battery cell.[9] Even though the first report on such a system dates back to the year 2000,[10] the rather poor irreversibility of the lithium plating and stripping have suppressed intensive research in this field—until very recently, Weber et al.,[11] Louli et al.,[12] and Lee et al.[13] reported an outstanding cycle life for such systems. Weber et al.[11] achieved 80% capacity retention after 90 cycles, utilizing an optimized liquid electrolyte containing two lithium salts, namely, 0.6 M $LiBF_4$ and 0.6 M lithium difluoro(oxalato)borate (LiDFOB), in a mixture of fluoroethylene carbonate and diethyl carbonate in a 1:2

volume ratio. The current collector was a bare copper foil, and the positive electrode was based on single-crystal Li-$Ni_{0.5}Mn_{0.3}Co_{0.2}O_2$ (NMC_{532}) as the active material. A further improvement was achieved by Louli et al.[12] via an optimization of the salt concentration. The high-concentration dual-salt electrolyte composed of 2.0 M LiDFOB and 1.4 M $LiBF_4$ enabled a substantially prolonged cycle life of up to 200 cycles with 80% capacity retention at 20 °C and under high pressure (1170 kPa). Lee et al.[13] reported a capacity retention of 89% after 1000 cycles for an all-solid-state "zero excess" lithium battery. In their work, the current collector was a stainless steel foil, coated with a thin layer of a carbon/silver nanocomposite, and the positive electrode was based on Ni-rich NMC as the active material. So far, the majority of research studies have focused on the optimization of the (liquid) electrolyte composition, e.g., by utilizing highly concentrated electrolytes,[14,15] localized high-concentration electrolytes,[16,17] and alternative dual-salt electrolytes;[18,19] or introducing suitable additives;[20] or the modification of the negative electrode current collector, for instance, by applying a polymer[21] or inorganic[22,23] coating on the current collector. In general, the reactions occurring at the negative electrode∣electrolyte

Scheme 1. Schematic Illustration of the Preparation of the [111]-Oriented Nanotwinned Copper Foil and Its Use in "Zero Excess" Lithium−Metal Batteries Comprising an NMC$_{811}$-Based Cathode
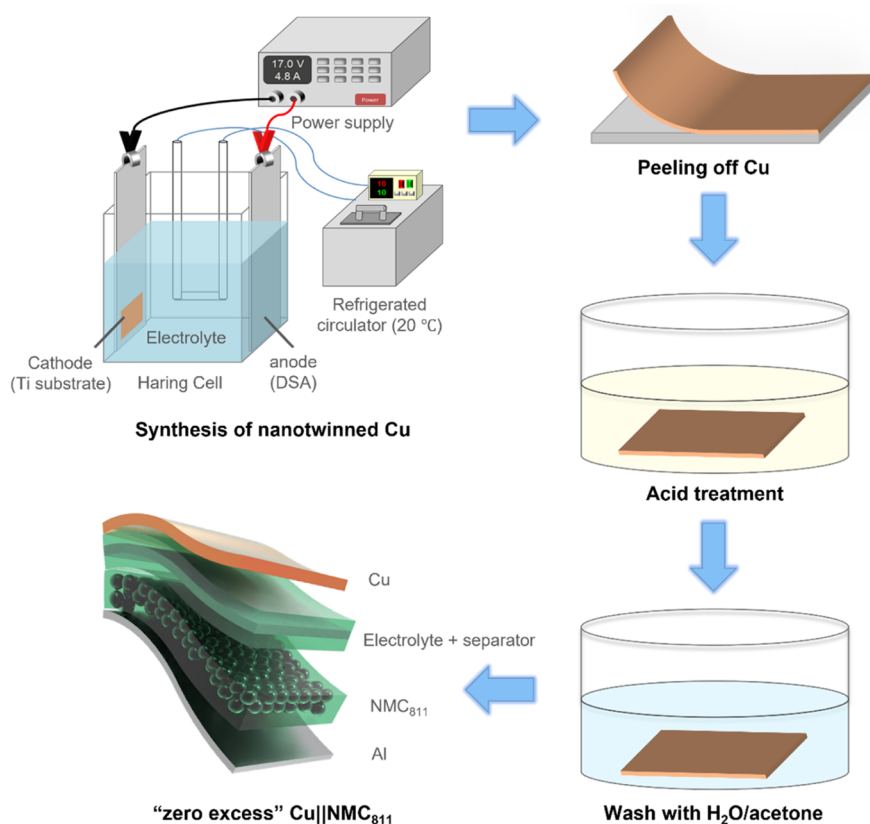
interface, including among others, the lithium nucleation and the formation of a long-term stable interphase, are essential for realizing long-term stable "zero excess" lithium−metal batteries. Focusing on the lithium nucleation on (and diffusion along) the current collector surface, Pande and Viswanathan[24] recently reported a theoretical study on a comparison of various metallic current collectors and lithium alloys. Generally, the lithium alloys showed very promising potential specific energies, low nucleation overpotential, and better rate capability. However, such alloys commonly react with the ambient atmosphere and would, thus, require the same or very similar processing conditions as lithium metal foils. Interestingly, they also reported a favorable adsorption energy for face-centered cubic (*fcc*) Cu(111) surfaces and a rather low energy barrier for lithium diffusion.[25] Studying single crystals, Ishikawa et al.[25] reported that the Cu(111) surface is also advantageous with regard to the formation of an electrolyte decomposition-related interphase with low resistivity. Common commercial copper foils, however, are characterized by a polycrystalline nature with a mosaic-like arrangement of [111]-, [200]-, and [220]-oriented nanocrystals,[26,27] and the cost-efficient realization of single-crystalline copper foils on the industrial scale appears rather unlikely. Nevertheless, polycrystalline copper foils with an essentially pure [111] orientation and dense twin boundaries, so-called nanotwinned copper foil,[28−31] can be fabricated using the existing electrodeposition techniques on a large scale and at a high production rate.[32] Such nanotwinned copper foil shows substantially enhanced mechanical strength and lower electronic resistance compared to randomly oriented copper foil, while visually resembling the conventional 2D morphology.[28−31]

Herein, we prepared nanotwinned copper foil following an earlier reported electrodeposition technique[33] and investigated its suitability as a current collector for the negative electrode in "zero excess" lithium−metal batteries in comparison with that of a conventional polycrystalline copper foil (Scheme 1). The results show that the [111]-oriented nanotwinned copper foils provide a much more homogeneous lithium deposition, suppressed dendrite formation, and superior cycling stability of Cu∥Li and Cu∥LiNi$_{0.8}$Mn$_{0.1}$Co$_{0.1}$O$_2$ (NMC$_{811}$) cells.

2. EXPERIMENTAL SECTION

2.1. Fabrication and Characterization of the Copper Foils.
Copper foils with dimensions of 15 × 6 cm^2 were prepared by electrodeposition, as reported very recently.[33] In brief, a finely polished titanium plate was employed as the cathode substrate in an 8.5 liter tank. The basic electrolyte contained 1.08 M CuSO$_4$•5H$_2$O (UniRegion Bio-Tech, electronic grade), 25 mM H$_2$SO$_4$ (Uni-Onward, 98%), 0.7 mM NaCl (Showa Chemical, 99%), and thiol organic additives to control the grain orientation of the electro-deposited copper foils. Two types of copper foils were prepared. A conventional copper foil with a polycrystalline texture was obtained by adding a gelatin-type additive in the basic electrolyte, and the nanotwinned copper foil with a [111]-oriented grain structure was realized by adding sodium 3-mercapto-1-propanesulfonate (MPS, ALDRICH, 90%). The thickness of the conventional and nano-twinned copper foils was about 35 μm.

The surface morphology of the two copper foils was examined by scanning electron microscopy (SEM) (ZEISS EVO MA 10 micro-scope) and atomic force microscopy (AFM) (Bruker Icon), including an estimation of the surface roughness. The crystal orientation was evaluated by X-ray diffraction (XRD) (Bruker D2 Phaser) in Bragg−Brentano geometry. The cross-sectional grain structure was studied by SEM and focused ion beam (FIB) (FEI Helios 600i) milling. X-ray
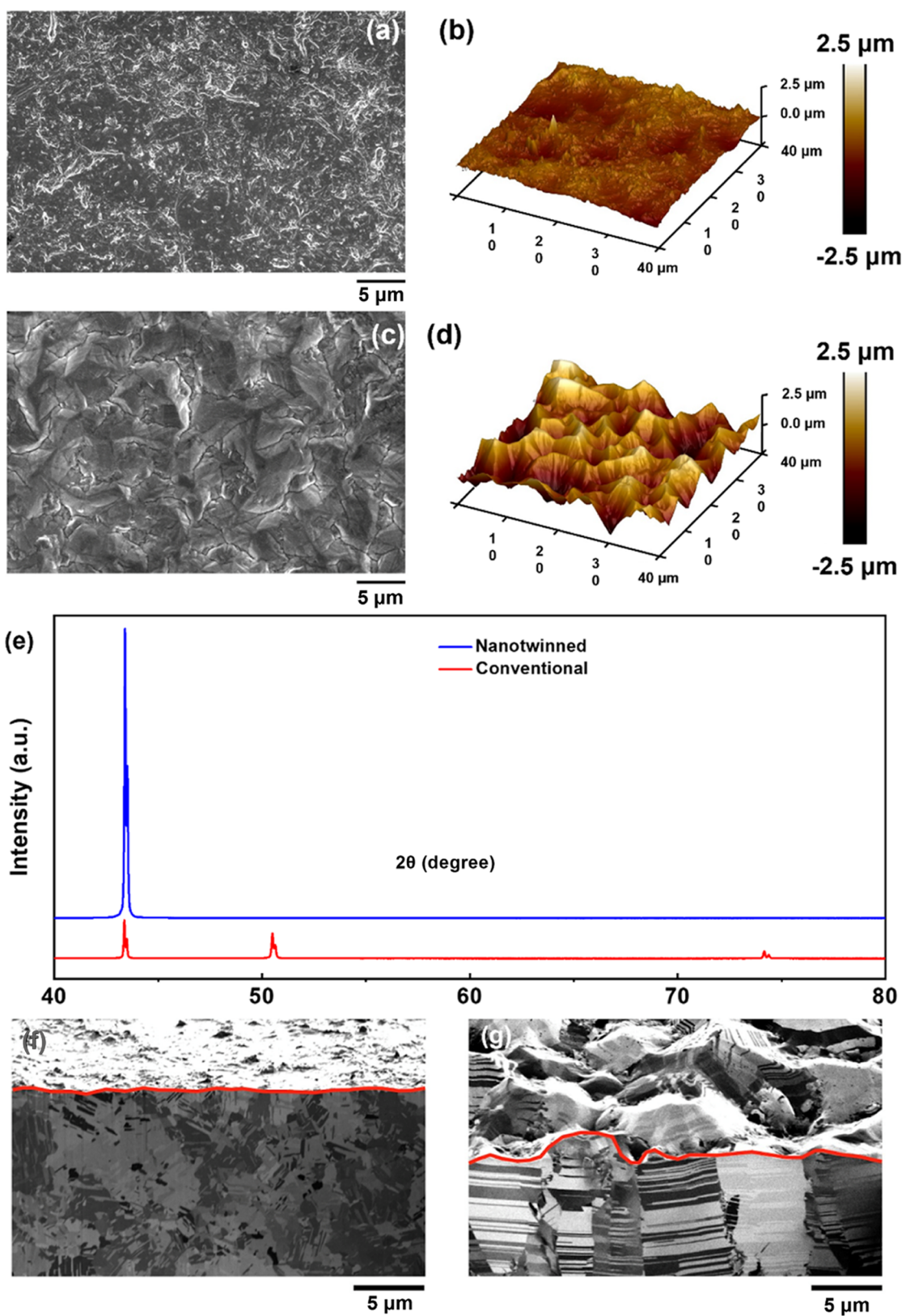
Figure 1. Examination of the surface morphology of (a,b) conventional and (c,d) [111]-oriented nanotwinned copper foil by means of (a,c) SEM and (b,d) AFM. In the latter case, the Z-axis scales were adjusted to ±2.5 μm. (e) XRD pattern of the conventional (in red) and nanotwinned (in blue) copper foil. As the inset, the amplified regions around 50.5 and 74.3° to highlight the (200) and (220) reflections, respectively, are shown (the two maxima in each case arise from the Cu K$_{\alpha1}$ and K$_{\alpha2}$ contributions of the X-ray tube). (f,g) Cross-sectional SEM analysis of the (f) conventional and (g) nanotwinned copper foil following FIB milling.

photoelectron spectroscopy (XPS) measurements were performed using a PHI 5800 MultiTechnique electron spectroscopy for chemical analysis system with monochromatized Al Kα radiation (1486.6 eV). The detection angle of the measurements was 45°, and pass energies of 93.9 and 29.35 eV were used for the survey and detailed spectra, respectively. The samples were neutralized with electrons from a flood gun (current ≈ 3 μA) to compensate for charging effects at the surface. The binding energies of all spectra were calibrated to the C 1s signal at 284.8 eV, which resulted in the F 1s peak of LiF which is very close to 685 eV in the ex situ spectra. The data were analyzed using CasaXPS software.

2.2. Calculation of the Texture Coefficient. Based on the XRD data, the texture coefficient (TC) was calculated to identify and quantify the crystal orientation of the two Cu foils. The TC values were estimated from the relative intensities of the XRD reflections using the following equation[26]

$$\text{TC}_{(hkl)} = \frac{I_{(hkl)}/I_{0(hkl)}}{(1/n)\sum I_{(hkl)}/I_{0(hkl)}}$$

where $I_{0(hkl)}$ and $I_{(hkl)}$ represent the relative intensities of the (hkl) reflections from the XRD reference data of a randomly oriented powder sample (JCPDS card number 04-0836). The value n is the number of the total planes. For copper, in our case, n is 3, as there are three reflections observed in the given 2θ range.

2.3. Electrode Preparation, Cell Assembly, and Electrochemical Characterization. Electrodes based on NMC$_{811}$ as the active material were prepared by mixing NMC$_{811}$ (92 wt %) with C-NERGY Super C65 (TIMCAL, 4 wt %) and poly(vinylidene difluoride) (PVdF, 6020, Solvay, 4 wt %) in an appropriate amount of N-methyl-2-pyrrolidone (NMP, Aldrich) using a slurry mixer (Wellcos). The resulting slurry was cast on aluminum foil utilizing a laboratory-scale doctor blade. Subsequently, the electrode sheets were pre-dried at 60 °C, and disc-shaped electrodes with a diameter of 12 mm were cut. These electrodes were further dried under vacuum at 100 °C for 12 h and had an average active material mass loading of about 15.3 mg cm^{-2}. The electrode preparation was conducted in a dry room with a dew point of less than −60 °C.

Cu∥Li and Cu∥NMC$_{811}$ coin cells (CR2032, Hohsen) were assembled in an argon-filled glovebox with oxygen and water contents lower than 0.1 ppm. The lithium foil was purchased from Honjo (battery grade, 500 μm thickness). The Asahi separator was drenched with 70 μL of a 1 M solution of LiPF$_6$ in a 1:1 (by weight) mixture of ethylene carbonate (EC) and dimethyl carbonate, purchased from UBE. Vinyl ethylene carbonate (VEC) (Sigma-Aldrich) was added to this electrolyte solution in a volume ratio of 15:85. The diameter of the lithium and NMC$_{811}$ electrodes was 12 mm, and the diameter of the copper foils was 14 mm in order to avoid any kind of "edge effects". The electrochemical characterization was conducted using a battery testing system (Maccor Series 4000). The cut-off voltages for the Cu∥NMC$_{811}$ coin cells were 3.0 and 4.3 V. The initial three formation cycles were performed at 0.1 C (1 C = 200 mA g^{-1}), and the subsequent cycling was conducted at a charge rate of 0.2 C and a discharge rate of 0.5 C. Cycled Cu∥Li and Cu∥NMC$_{811}$ cells were disassembled in an argon-filled glovebox, and the lithium morphology electrodeposited on the different copper foils was examined by SEM. The samples were transferred to SEM using an argon-filled sample transfer shuttle (SEMILAB) to avoid any contact with air or moisture.

2.4. Density Functional Theory Calculations. Periodic density functional theory (DFT) calculations were conducted using the Vienna ab initio simulation package (VASP).[34] VASP is a plane wave code, using pseudopotentials to describe the electron−core interaction. For the calculations, the projector-augmented wave method was applied,[35] with exchange and correlation being accounted for by the generalized gradient approximation as introduced by Perdew, Burke, and Ernzerhof.[36] The investigated surfaces were built with three or more layers with the top-most layer freely relaxed, while the bottom layers were fixed to the bulk structure. Above the surface, a vacuum layer of at least 12 Å was added to hinder spurious self-interactions. All calculations were conducted with a plane wave cut-off

energy of 500 eV and either a $7 \times 7 \times 1$ [(111) and (100) surface] or a $7 \times 5 \times 1$ [(110) surface] k-point mesh, adapted to the supercell size. The adsorption energies were obtained as $E_{\text{ads}} = E_{\text{adsorbed}} - E_{\text{clean}} - E_{\text{Li}}$ with E_{adsorbed}, E_{clean}, and E_{Li} being the energy of the surface with a Li atom adsorbed, the energy of the clean surface, and the energy of a Li atom as a reference, respectively. Note that a more negative adsorption energy corresponds to a stronger adsorption. To investigate the diffusion barriers for adatom diffusion on the respective surfaces, the climbing image nudged elastic band (NEB) method was applied.[37,38]

3. RESULTS AND DISCUSSION

In a first step, the surface morphology of the two copper foils, i.e., the conventional polycrystalline and the [111]-oriented nanotwinned copper foil, was examined via SEM and AFM (Figure 1). The SEM micrograph of the conventional Cu foil is presented in Figure 1a. The surface is rather smooth without any significant surface undulation and comparable to that of most commercial Cu foils, resembling the copper foil produced by the rolling method.[32] In Figure 1c, the SEM micrograph of the nanotwinned Cu foil is displayed. Unlike that of the conventional Cu foil, the surface is characterized by cone-like features, comparable to previous studies.[28,30] The corresponding AFM data are presented in Figure 1b,d. In agreement with the SEM analysis, the surface of the conventional Cu foil is generally much flatter. The arithmetic average surface roughness, Ra, was 0.19 and 0.55 μm for the conventional and the nanotwinned Cu foil, respectively. The cone-like features observed for the nanotwinned Cu foil originate from an out-of-plane grain rotation, driven by the reduction of the grain boundary energy.[39] Such a relatively rougher surface might have a beneficial impact on the reversibility of the lithium deposition as reported by Gu et al.[40] for stainless steel current collectors.

In a second step, the crystal orientation of the two Cu foils was determined. Figure 1e shows the XRD patterns of both Cu foils, with a magnification of the regions around 50.5 and 74.3°; i.e., the regions where the (200) and (220) Bragg reflections, respectively, commonly occur. The conventional foil exhibits the common three (111), (200), and (220) Bragg reflections, confirming the polycrystalline nature of the foil, showing random orientation. Differently, the nanotwinned Cu foil reveals only a very intense (111) reflection and (essentially) no diffraction intensity in the regions of the other two reflections. The TC derived from the XRD results was calculated, revealing 0.89, 1.27, and 0.84 for TC$_{(111)}$, TC$_{(200)}$, and TC$_{(220)}$, respectively, for the conventional Cu foil, indicating a slightly preferred [200] orientation, while the other two orientations were still very prominent. For the nanotwinned Cu foil, the TC$_{(111)}$ value is 2.97, and TC$_{(200)}$ and TC$_{(220)}$ are essentially 0 (<0.02), implying that the nanotwinned Cu foil is characterized essentially by a pure [111] grain orientation. In Figure 1f,g, the ion-channeling images of the cross-section of the conventional and nanotwinned Cu foils, respectively, are displayed. The red lines indicate the boundary between the cross-section and the surface, once more confirming that the nanotwinned Cu foil is characterized by a much more pronounced surface undulation. The crystalline microstructure of the conventional Cu foil (Figure 1f) does not exhibit an ordered pattern but rather a random orientation and the typical high-angle grain boundaries. Consequently, the grains exposed to the surface have different crystal orientations, presumably [111], [200], and [220] following the XRD data. In fact, the surface energy of the

different crystal orientations decreases in the order [220] > [200] > [111],[41] in line with the intensity of the XRD reflections and results from DFT, as discussed below. The grain size in the vicinity of the surface is in the range from 0.3 to 1.4 μm. For the nanotwinned Cu foil (Figure 1g), the ion-channeling images of the cross-section reveal rather regular twin boundaries between the columnar grains, and the cone-like features at the surface reflect a clear twin boundary microstructure, indicating that the exposed surface follows the highly oriented crystalline nature of the cross-section.

In sum, the XRD and SEM/FIB results confirm the successful synthesis of a conventional polycrystalline and a highly [111]-oriented nanotwinned copper foil. It appears noteworthy that the high-angle grain boundaries observed for the conventional Cu foil have a higher energy than the nanotwinned grain boundaries and are more prone to defects.[31] Moreover, the homogeneous nature of the grain boundaries of the nanotwinned Cu foil might play an important role in the lithium deposition since the nucleation of heterogeneous materials preferably occurs at the grain boundaries.[42] Accordingly, a more homogeneous lithium deposition is expected for the nanotwinned Cu foil.

To confirm this, Cu‖Li cells were assembled and subjected to a series of electrochemical tests. The electrolyte comprised 15 vol % of VEC, following a previous study by Yang et al.,[43] who reported an advantageous impact on lithium metal electrodes. In fact, the cells comprising VEC revealed a substantially higher and more stable CE compared to the VEC-free electrolyte upon continuous lithium plating and stripping (Figure S1). For the comparison of the conventional and the nanotwinned Cu foils, the investigation focused on the homogeneity and morphology of the electrochemically deposited lithium, applying different current densities of 0.25, 0.5, and 2 mA cm^{-2} while fixing the total capacity to 1 mAh cm^{-2}. At a relatively low current density of 0.25 mA cm^{-2} (Figure 2), the conventional Cu foil reveals an island-like lithium deposition with a rather large portion of bare Cu foil still being visible (Figure 2a). The magnification shows that the majority of the lithium grains have a size of several micrometers with an irregular shape, but there are also some needle-like deposits (Figure 2b). Differently, the lithium coverage on the nanotwinned copper foil is much more
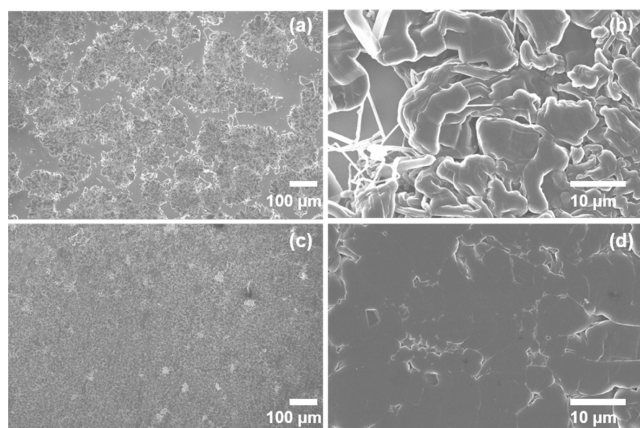

Figure 2. SEM analysis of the lithium morphology at different magnifications after deposition on (a,b) conventional and (c,d) nanotwinned copper foil, applying a current density of 0.25 mA cm^{-2} with a total capacity of 1 mA h cm^{-2}.

homogeneous with only a few spots of bare copper foil still being exposed (Figure 2c). At higher magnification (Figure 2d), a very dense lithium morphology becomes apparent, and the boundaries between the different lithium grains are essentially invisible, as the grains are highly merged. No needle-like deposits could be detected.

Increasing the current density to 0.5 mA cm^{-2} resulted generally in a more homogeneous lithium deposition for both copper foils (Figure 3). For the conventional foil, there are still
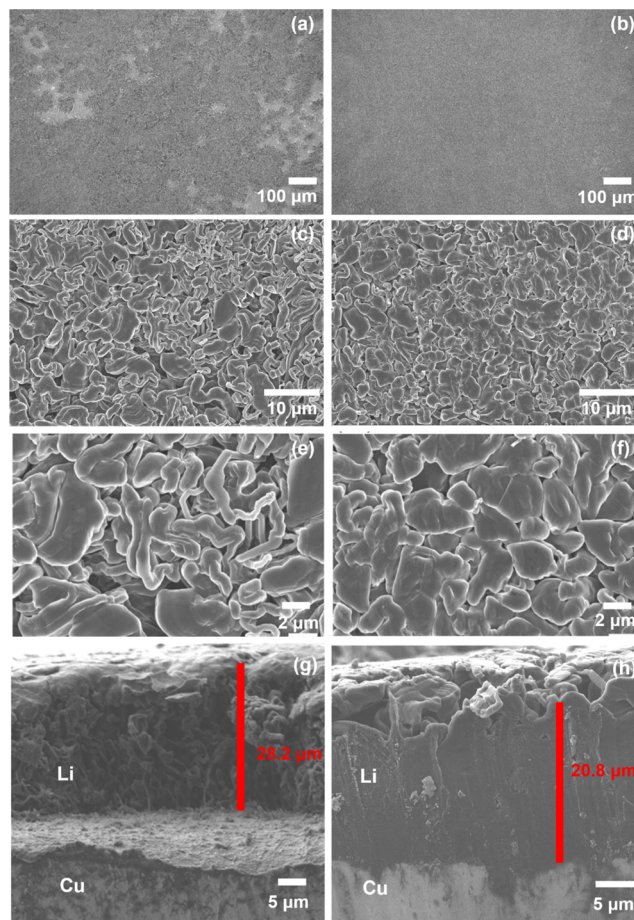

Figure 3. SEM analysis of the lithium morphology at different magnifications for (a,c,e) conventional Cu foil and (b,d,f) nanotwinned Cu foil. (g,h) SEM micrographs of the corresponding cross-section for (g) conventional and (h) nanotwinned Cu foil. The lithium was deposited at a current density of 0.5 mA cm^{-2} with a total capacity of 1 mA h cm^{-2}.

some spots of bare copper observed (Figure 3a), while the lithium deposition on the nanotwinned Cu foil appears fully homogeneous (Figure 3b). In fact, this difference is already visible with naked eyes, as illustrated by the photographs of the two Cu foils (Figure S2). The SEM micrographs at higher magnifications (Figure 3c−f) reveal that in both cases, the lithium grain size is in the order of 2−5 μm.

However, for the conventional Cu foil, a significant fraction of needle-/worm-like lithium deposits with a diameter of less than 1 μm is observed (Figure 3c,e), which are essentially absent for the nanotwinned foil (Figure 3d,f). Moreover, it appears that the lithium grains are packed in a denser fashion on the nanotwinned Cu foil compared to those on the conventional one. The analysis of the cross-section confirms

the abovementioned, revealing a lithium layer thickness of ca. 28.2 μm for the conventional foil (Figure 3g) and about 20.8 μm for the nanotwinned one (Figure 3h). As seen from Figure S3a,b, part of the deposited lithium is detached from the conventional Cu foil, whereas an intimate contact between deposited lithium and nanotwinned Cu foil is evidenced in Figure S3c. Therefore, the contact between the lithium film and the copper current collector appears much better for the nanotwinned Cu foil.

When increasing the current density further to 2 mA cm^{-2}, the homogeneity of the lithium deposition further increases, as apparent from the low-magnification SEM micrographs, though it still remains inferior for the conventional Cu foil (Figure 4a) compared to that for the nanotwinned one (Figure
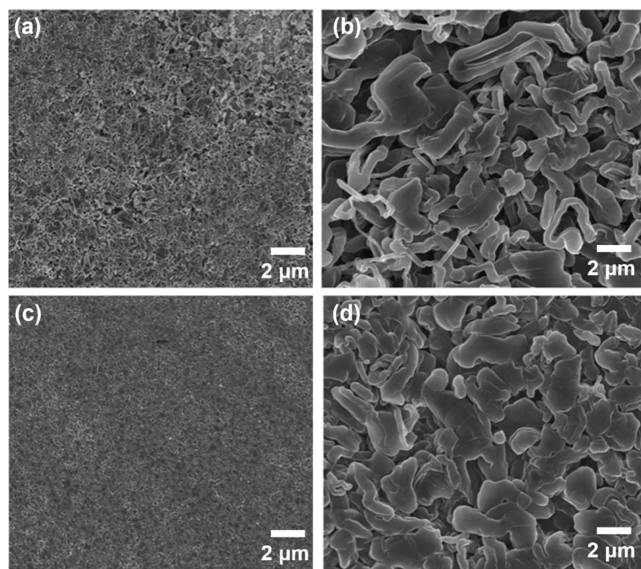

Figure 4. SEM analysis of the lithium morphology at different magnifications after deposition on (a,b) conventional and (c,d) nanotwinned copper foil, applying a current density of 2.0 mA cm^{-2} with a total capacity of 1 mA h cm^{-2}.

4c). At the same time, however, the presence of needle- and worm-like lithium deposits on the conventional foil increases (Figure 4b). In contrast, the lithium grains on the nanotwinned foil are larger (Figure 4d)—even though generally decreasing in size to a few μm—but no needle- and worm-like features are observed. The increasing homogeneity and decreasing grain size trend with increasing current densities is in agreement with the literature,[44] indicating that the lithium diffusion along the current collector surface is critical for the growth of larger grains, while the lithium nucleation is rather kinetically controlled. The comparison of the two foils, moreover, confirms that both the adsorption energy and the lithium diffusion energy barrier are lower for the (111) surface compared to those for the other two copper surfaces.[24]

This is further corroborated by DFT calculations for the (100), (110), and (111) surfaces of Cu. The (111) surface is not only the energetically most favorable surface but shows also the strongest lithium adsorption with -2.42 eV for a single lithium atom, whereas -2.31 eV for the Cu(110) surface and -2.20 eV for the Cu(100) surface are observed. Additionally, the diffusion barriers for Li atoms moving on the respective surfaces have been determined via the NEB method. The calculated barriers for a Li atom diffusing from one stable site

to the adjacent one on the three different Cu surfaces revealed the lowest value for the (111) surface which was less than 0.02 eV (Figure 5). Significantly larger values of 0.13 and 0.17 eV
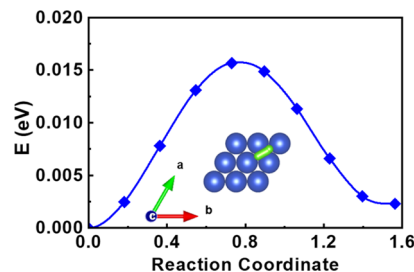

Figure 5. Minimum energy path for the Li diffusion on the Cu(111) surface between two adjacent surface sites, i.e., an fcc site and an hcp site. Note that the energies for these two sites are not equivalent, which is the consequence of differences in the underlying layer. As the inset, the corresponding diffusion pathway on the surface is shown [only the top-most Cu layer (in blue) and the diffusing Li (in green) are shown].

were calculated for the (110) and (100) surfaces, respectively (Figure S4). Hence, the DFT calculations indicate a clear adsorption preference for the (111) surface, which, moreover, shows by far the fastest kinetics. Fast surface kinetics allow for facile Li motion on the surface and, therefore, are a prerequisite for a smooth growth of the deposited layer.

To evaluate whether these advantageous properties of the [111] oriented-nanotwinned copper foil persist also upon continuous lithium plating and stripping, Cu‖Li half-cells, comprising either the conventional or the nanotwinned Cu foil, were subjected to galvanostatic cycling. First, employing an applied current density of 0.5 mA cm^{-2}, a Li plating step was performed up to a total capacity of 1 mA h cm^{-2}. The results are summarized in Figure 6a−c.

The CE vs cycle number plot is depicted in Figure 6a. For the conventional foil, the CE is rather stable for about 35 cycles but then rapidly decays, accompanied by a severe fluctuation, indicating the formation of dendritic lithium, in line with the previous findings. For the nanotwinned Cu foil, the CE is generally somewhat higher at about 98% and much more stable, especially for the initial 80 cycles, before it slightly decreases but without the severe fluctuation observed for the conventional foil. This is also reflected by the significantly higher average CE of 95.9% for the 100th−235th cycles compared to only 93.2% for the conventional foil. In addition, the voltage profile of the first lithium plating reveals a lower plateau overpotential (η_p) for the nanotwinned Cu foil of approximately -0.053 V vs -0.073 V (Figure 6b). Given that the electronic conductivity of the copper foil is essentially unaffected by the nanotwinned structure,[28,45] a lower plateau's overpotential indicates a smaller kinetic barrier of the liquid to solid phase transition.[46] Since this is also linked to the available surface sites and the faster lithium diffusion,[47] it is well in line with the more homogeneous lithium deposition that we observed for the nanotwinned Cu foil and the facilitated lithium diffusion along the (111) Cu surface. Nonetheless, the initial nucleation overpotential (η_n) of -0.138 V is essentially the same for the two foils. This finding might indicate that in both cases, the initial nucleation occurs on the same surface facets, i.e., the (111) surfaces, which would also provide an explanation for the inhomogeneous lithium deposition on the conventional Cu foil. Pei et al.[44] have reported that the grain
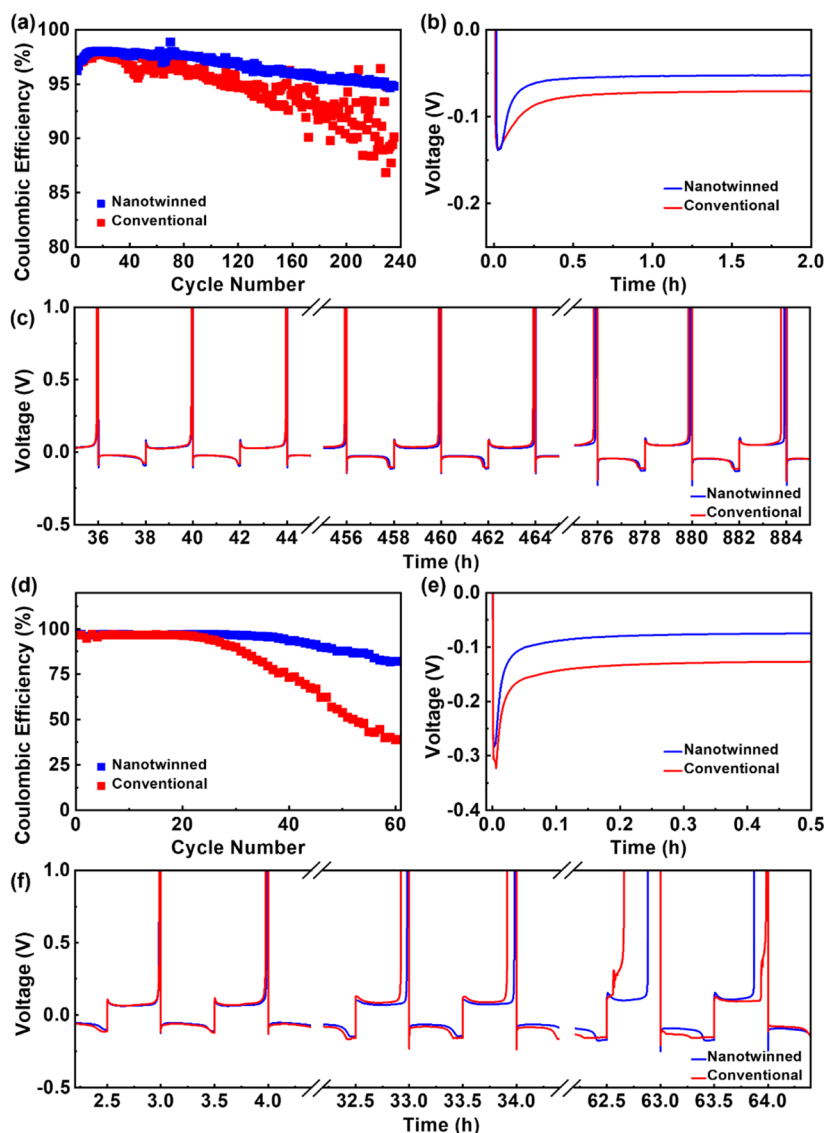
Figure 6. Performance of Cu‖Li cells assembled using the conventional (red) or nanotwinned (blue) copper foil, cycled at (a−c) current density of 0.5 mA cm^{-2} with a total capacity of 1 mA h cm^{-2} and (d−f) current density of 2.0 mA cm^{-2} with a total capacity of 1 mA h cm^{-2}. (a,d) Plot of the CE; (b,e) evolution of the potential during the first lithium deposition; and (c,f) plot of the potential evolution upon continuous plating and stripping for selected cycles. The cut-off voltage for the stripping step was set to 1.0 V.

size of the electrodeposited lithium shows an inverse relationship with η_p; i.e., the lower the η_p, the larger the grain size. This is in excellent agreement with the findings obtained from the SEM analysis discussed above (Figure 3). In Figures 6c and S5a, selected voltage profiles for the continuous plating and stripping are presented. It is observed that the voltage hysteresis for the plating/stripping process gradually increases upon cycling for both foils by about 65 and 53 mV after 460 h (i.e., about 115 cycles) for the conventional and nanotwinned Cu foils, respectively. Furthermore, the amount of reversibly stripped lithium becomes increasingly smaller for the conventional foil, as very evident from the shortening of the plateau after about 220 cycles, suggesting an increasing formation of dead lithium. In fact, it has been reported earlier that the shape of the lithium grains is a critical factor for the plating/stripping reversibility with needle-like deposits especially favoring poor CEs compared to granular lithium deposits.[48] The same trends were generally observed when increasing the current density to 2.0 mA cm^{-2} (Figure 6d−f).

The CE started decreasing a little earlier, though, and the decay was particularly pronounced for the conventional foil (Figure 6d). The plot of the voltage evolution during the initial plating resembles the same trend as that seen when applying a lower current density of 0.5 mA cm^{-2} (Figure 6e). Nevertheless, at 2.0 mA cm^{-2}, η_n is slightly lower for the nanotwinned Cu foil. Considering the much more homogeneous lithium deposition at such high current density also in the case of the conventional foil (Figure 4a), this observation suggests that now lithium is also nucleating on the other two surface facets, which are characterized by less favorable adsorption energies. The voltage profiles for the subsequent cycles (Figures 6f and S5b) further corroborate the superior performance of the nanotwinned Cu foil, and the trend of the faster hysteresis increase and shortening of the lithium stripping plateau is even more pronounced for the conventional Cu foil at this higher current density.

In order to test whether this superior behavior of the [111]-oriented nanotwinned copper foil is related to the beneficial
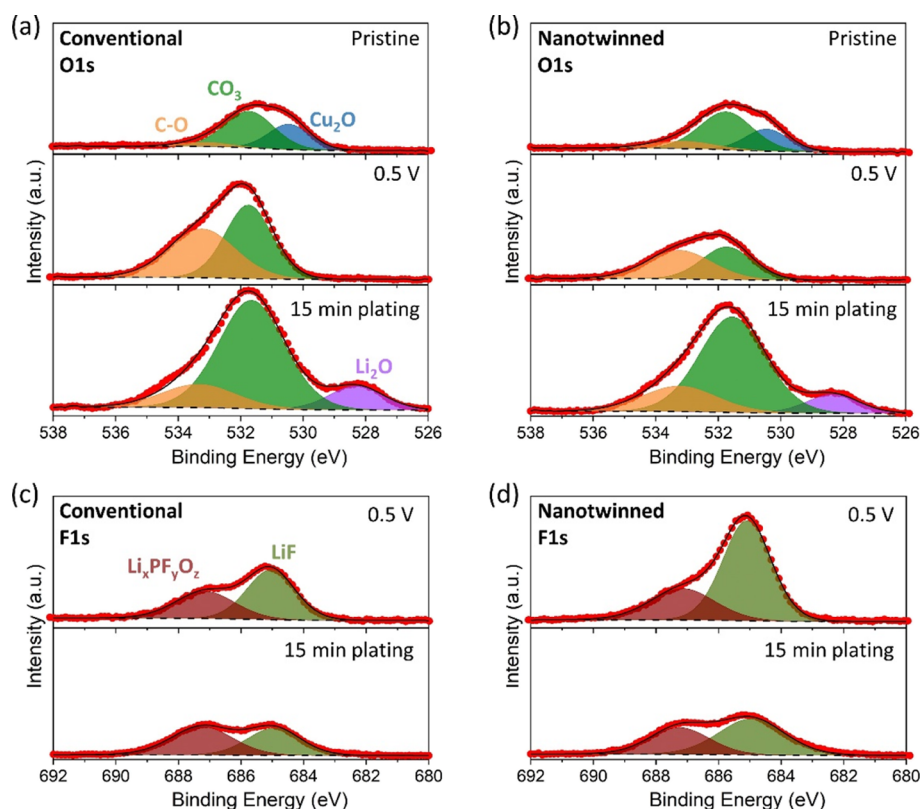
Figure 7. XPS analysis for the pristine electrodes (no contact with the electrolyte) at 0.5 V and after 15 min of lithium plating (initial lithiation). (a,b) Oxygen 1s region for (a) conventional and (b) [111]-oriented nanotwinned copper foil. (c,d) Fluorine 1s region for the same samples (without the pristine ones).

impact on the electrolyte decomposition-related interphase, as reported by Ishikawa et al.,[25] an *ex situ* analysis of the two different copper foils via XPS was performed. Spectra were collected for the pristine foils, at a cut-off voltage of 0.5 V, and after 15 min of lithium plating, i.e., after the onset of electrolyte decomposition, but before lithium plating (0.5 V), and after the onset of lithium metal nucleation. The spectra in the Cu2p region (Figure S6a,b) show mainly metallic copper and Cu_2O in the pristine state. The Cu peaks then gradually decrease in intensity at 0.5 V due to the formation of the electrolyte decomposition-related interphase and vanish after 15 min as a result of the additional lithium plating on the Cu surface. This trend appears to be the same for both Cu foils.

The spectra in the O1s region of the conventional Cu foil in Figure 7a show contributions of Cu_2O[49] and carbonate residues, presumably from the ambient atmosphere. At 0.5 V, the signal of Li_2CO_3 and C–O dominates the spectrum, indicating the reduction of the electrolyte.[50] After 15 min of lithium plating, the spectrum additionally shows a contribution from Li_2O. Essentially, the same trend is observed also in the case of the nanotwinned Cu foil (see Figure 7b). However, the intensity of the organic species at 0.5 V is significantly smaller, indicating a less pronounced reduction of the organic carbonate solvents in this case. On the other hand, the F1s spectra (Figure 7c,d) show a significantly higher LiF signal at 685 eV[50] in the case of the nanotwinned Cu at 0.5 V, which points to a more pronounced reduction of the conducting salt on the nanotwinned Cu surface at these potentials. This observation is confirmed by the Li1s spectra displayed in Figure S6c,d. Such relatively greater decomposition of the conducting salt over the organic solvents is in line with the

favorable lithium adsorption at the (111) surface and presumably adds to the favorable lithium plating/stripping behavior. In fact, a LiF-rich solid electrolyte interphase (SEI) has been proven to be beneficial for homogeneous and reversible lithium deposition and stripping.[5,51] Nonetheless, the differences between the two Cu foils are not that pronounced, especially after 15 min of lithium plating, where both foils reveal very similar spectra, suggesting that the substantially enhanced electrochemical performance of the [111]-oriented nanotwinned Cu foil compared to that of conventional Cu is at least partially or maybe largely related to the more favorable lithium adsorption and diffusion on the nanotwinned Cu foil.

Eventually, the performance of the two Cu foils was tested in "zero excess" Cu||NMC$_{811}$ full cells (Figure 8). Figure 8a,b shows SEM micrographs of the lithium deposited on the conventional and nanotwinned Cu foils, respectively, after the first charge. A charge rate of 0.1 C in the first cycles corresponds to a current density of about 0.3 mA cm^{-2}, i.e., in the same range as that for the previous tests.

The nanotwinned Cu foil reveals a denser lithium deposition and the formation of rather granular lithium grains, while several needle-like lithium deposits are observed for the conventional Cu foil. This beneficial effect is reflected also by the superior CE upon continuous cycling and the consequently delayed capacity fading (Figure 8c), while the first cycle discharge capacity and CE are essentially the same for the two cells at about 205 mA h g^{-1} and 92.8%, respectively. The average CE for the 5th–40th cycles, however, is 97.0 and 97.9% for the conventional and nanotwinned copper foils, respectively (a magnification of the CE is provided in Figure
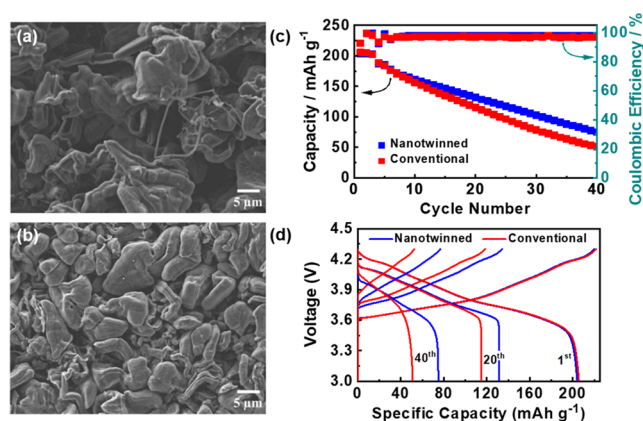
Figure 8. SEM micrographs of the morphology of metallic lithium deposited on (a) conventional and (b) nanotwinned copper foil obtained from the Cu‖NMC$_{811}$ cells cycled at 0.1 C. (c) Evolution of the discharge capacity and CE of these cells employing the conventional (in red) and nanotwinned (in blue) copper foils. The C rate for the initial three formation cycles was 0.1 C, followed by continuous cycling with a charge and discharge rate of 0.2 and 0.5 C, respectively. The cut-off voltages were set to 3.0 and 4.3 V. (d) Plot of the corresponding dis-/charge profiles for the 1st, 20th, and 40th cycles.

S7). The average CE of nanotwinned copper foil is still lower than that of state-of-the-art lithium-ion batteries (>99.9%), indicating that there is a significant lithium loss and electrolyte decomposition occurring at each cycle, as also reflected by the continuous capacity decrease upon cycling. Nonetheless, these detrimental phenomena are less pronounced for the [111]-oriented nanotwinned Cu foil than those for the conventional Cu foil. Accordingly, the discharge capacity for the 40th cycle is 75 mA h g^{-1} for the nanotwinned Cu and only 51 mA h g^{-1} for the conventional foil, i.e., 34% higher. The corresponding voltage profiles, depicted in Figure 8d, show that the superior performance of the nanotwinned Cu foil is largely related to a lower overpotential for the charge process, presumably originating from a greater formation of electronically insulating dead lithium on the conventional Cu foil.

4. CONCLUSIONS

A [111]-oriented nanotwinned copper foil was prepared using a scalable electrodeposition process. Its performance in "zero excess" lithium−metal batteries has been investigated and compared with that of polycrystalline copper foil characterized by the rather random crystal orientation. The exclusive exposure of the rougher Cu(111) surface favors a homogeneous lithium nucleation and the growth of larger and denser lithium deposits and a LiF-richer interphase, which results in an enhanced reversibility of the lithium plating and stripping and a lower overpotential—a trend that is increasingly pronounced at elevated current densities. These beneficial properties translate also in a greater CE and improved capacity retention by about 34% after 40 cycles of "zero excess" Cu‖NMC$_{811}$ full cells. We may anticipate that these findings will trigger further research on highly oriented current collector surfaces—an approach that is highly complementary to the research and development efforts toward stabilizing artificial interlayers and optimized electrolyte compositions, as also shown herein.

AUTHOR INFORMATION

Corresponding Authors

Stefano Passerini − *Helmholtz Institute Ulm (HIU), Ulm 89081, Germany; Karlsruhe Institute of Technology (KIT), Karlsruhe 76021, Germany;* orcid.org/0000-0002-6606-5304; Email: stefano.passerini@kit.edu

Chi-Chang Hu − *Department of Chemical Engineering, National Tsing Hua University, Hsin-Chu 30013, Taiwan;* orcid.org/0000-0002-4308-8474; Email: cchu@che.nthu.edu.tw

Dominic Bresser − *Helmholtz Institute Ulm (HIU), Ulm 89081, Germany; Karlsruhe Institute of Technology (KIT), Karlsruhe 76021, Germany;* orcid.org/0000-0001-6429-6048; Email: dominic.bresser@kit.edu

Authors

Chun-Cheng Lin − *Department of Chemical Engineering, National Tsing Hua University, Hsin-Chu 30013, Taiwan*

Zhen Chen − *Helmholtz Institute Ulm (HIU), Ulm 89081, Germany; Karlsruhe Institute of Technology (KIT), Karlsruhe 76021, Germany*

Holger Euchner − *Institute of Theoretical Chemistry, Ulm University, Ulm D-89081, Germany; Institute of Physical and Theoretical Chemistry, University of Tübingen, Tübingen 72076, Germany;* orcid.org/0000-0003-2287-6970

Tobias Eisenmann − *Helmholtz Institute Ulm (HIU), Ulm 89081, Germany; Karlsruhe Institute of Technology (KIT), Karlsruhe 76021, Germany*

Katrin Geng − *Helmholtz Institute Ulm (HIU), Ulm 89081, Germany; Karlsruhe Institute of Technology (KIT), Karlsruhe 76021, Germany;* orcid.org/0000-0003-4347-4225

Thomas Diemant − *Helmholtz Institute Ulm (HIU), Ulm 89081, Germany; Karlsruhe Institute of Technology (KIT), Karlsruhe 76021, Germany*

Shan Fang − *Helmholtz Institute Ulm (HIU), Ulm 89081, Germany; Karlsruhe Institute of Technology (KIT), Karlsruhe 76021, Germany*

Chih-Han Yen − *Department of Chemical Engineering, National Tsing Hua University, Hsin-Chu 30013, Taiwan*

Author Contributions

C.-C.L. and Z.C. contributed equally to this study. The manuscript was written through contributions of all authors.

Notes

The authors declare no competing financial interest.

REFERENCES

(1) Bresser, D.; Hosoi, K.; Howell, D.; Li, H.; Zeisel, H.; Amine, K.; Passerini, S. Perspectives of Automotive Battery R&D in China, Germany, Japan, and the USA. *J. Power Sources* **2018**, *382*, 176−178.

(2) Marinaro, M.; Bresser, D.; Beyer, E.; Faguy, P.; Hosoi, K.; Li, H.; Sakovica, J.; Amine, K.; Wohlfahrt-Mehrens, M.; Passerini, S. Bringing Forward the Development of Battery Cells for Automotive Applications: Perspective of R&D Activities in China, Japan, the EU and the USA. *J. Power Sources* **2020**, *459*, 228073.

(3) Lin, D.; Liu, Y.; Cui, Y. Reviving the Lithium Metal Anode for High-Energy Batteries. *Nat. Nanotechnol.* **2017**, *12*, 194−206.

(4) Liu, J.; Bao, Z.; Cui, Y.; Dufek, E. J.; Goodenough, J. B.; Khalifah, P.; Li, Q.; Liaw, B. Y.; Liu, P.; Manthiram, A.; Meng, Y. S.; Subramanian, V. R.; Toney, M. F.; Viswanathan, V. V.; Whittingham, M. S.; Xiao, J.; Xu, W.; Yang, J.; Yang, X.-Q.; Zhang, J.-G. Pathways for Practical High-Energy Long-Cycling Lithium Metal Batteries. *Nat. Energy* **2019**, *4*, 180−186.

(5) He, X.; Bresser, D.; Passerini, S.; Baakes, F.; Krewer, U.; Lopez, J.; Mallia, C. T.; Shao-Horn, Y.; Cekic-Laskovic, I.; Wiemers-Meyer, S.; Soto, F. A.; Ponce, V.; Seminario, J. M.; Balbuena, P. B.; Jia, H.; Xu, W.; Xu, Y.; Wang, C.; Horstmann, B.; Amine, R.; Su, C.-C.; Shi, J.; Amine, K.; Winter, M.; Latz, A.; Kostecki, R. The Passivity of Lithium Electrodes in Liquid Electrolytes for Secondary Batteries. *Nat. Rev. Mater.* **2021**, *6*, 1036−1052.

(6) Hobold, G. M.; Lopez, J.; Guo, R.; Minafra, N.; Banerjee, A.; Shirley Meng, Y.; Shao-Horn, Y.; Gallant, B. M. Moving beyond 99.9% Coulombic Efficiency for Lithium Anodes in Liquid Electrolytes. *Nat. Energy* **2021**, *6*, 951−960.

(7) Schmuch, R.; Wagner, R.; Hörpel, G.; Placke, T.; Winter, M. Performance and Cost of Materials for Lithium-Based Rechargeable Automotive Batteries. *Nat. Energy* **2018**, *3*, 267−278.

(8) Duffner, F.; Kronemeyer, N.; Tübke, J.; Leker, J.; Winter, M.; Schmuch, R. Post-Lithium-Ion Battery Cell Production and Its Compatibility with Lithium-Ion Cell Production Infrastructure. *Nat. Energy* **2021**, *6*, 123−134.

(9) Nanda, S.; Gupta, A.; Manthiram, A. Anode-Free Full Cells: A Pathway to High-Energy Density Lithium-Metal Batteries. *Adv. Energy Mater.* **2020**, *11*, 2000804.

(10) Neudecker, B. J.; Dudney, N. J.; Bates, J. B. "Lithium-Free" Thin-Film Battery with In Situ Plated Li Anode. *J. Electrochem. Soc.* **2000**, *147*, 517.

(11) Weber, R.; Genovese, M.; Louli, A. J.; Hames, S.; Martin, C.; Hill, I. G.; Dahn, J. R. Long Cycle Life and Dendrite-Free Lithium Morphology in Anode-Free Lithium Pouch Cells Enabled by a Dual-Salt Liquid Electrolyte. *Nat. Energy* **2019**, *4*, 683−689.

(12) Louli, A. J.; Eldesoky, A.; Weber, R.; Genovese, M.; Coon, M.; deGooyer, J.; Deng, Z.; White, R. T.; Lee, J.; Rodgers, T.; Petibon, R.; Hy, S.; Cheng, S. J. H.; Dahn, J. R. Diagnosing and Correcting Anode-Free Cell Failure via Electrolyte and Morphological Analysis. *Nat. Energy* **2020**, *5*, 693−702.

(13) Lee, Y.-G.; Fujiki, S.; Jung, C.; Suzuki, N.; Yashiro, N.; Omoda, R.; Ko, D.-S.; Shiratsuchi, T.; Sugimoto, T.; Ryu, S.; Ku, J. H.; Watanabe, T.; Park, Y.; Aihara, Y.; Im, D.; Han, I. T. High-energy long-cycling all-solid-state lithium metal batteries enabled by silver-carbon composite anodes. *Nat. Energy* **2020**, *5*, 299−308.

(14) Qian, J.; Adams, B. D.; Zheng, J.; Xu, W.; Henderson, W. A.; Wang, J.; Bowden, M. E.; Xu, S.; Hu, J.; Zhang, J.-G. Anode-Free Rechargeable Lithium Metal Batteries. *Adv. Funct. Mater.* **2016**, *26*, 7094−7102.

(15) Nilsson, V.; Kotronia, A.; Lacey, M.; Edström, K.; Johansson, P. Highly Concentrated LiTFSI-EC Electrolytes for Lithium Metal Batteries. *ACS Appl. Energy Mater.* **2020**, *3*, 200−207.

(16) Ren, X.; Zou, L.; Cao, X.; Engelhard, M. H.; Liu, W.; Burton, S. D.; Lee, H.; Niu, C.; Matthews, B. E.; Zhu, Z.; Wang, C.; Arey, B. W.; Xiao, J.; Liu, J.; Zhang, J.-G.; Xu, W. Enabling High-Voltage Lithium-Metal Batteries under Practical Conditions. *Joule* **2019**, *3*, 1662−1676.

(17) Su, L.; Charalambous, H.; Cui, Z.; Manthiram, A. High-efficiency, anode-free lithium-metal batteries with a close-packed homogeneous lithium morphology. *Energy Environ. Sci.* **2022**, *15*, 843−854.

(18) Beyene, T. T.; Bezabh, H. K.; Weret, M. A.; Hagos, T. M.; Huang, C.-J.; Wang, C.-H.; Su, W.-N.; Dai, H.; Hwang, B.-J. Concentrated Dual-Salt Electrolyte to Stabilize Li Metal and Increase Cycle Life of Anode Free Li-Metal Batteries. *J. Electrochem. Soc.* **2019**, *166*, A1501−A1509.

(19) Alvarado, J.; Schroeder, M. A.; Pollard, T. P.; Wang, X.; Lee, J. Z.; Zhang, M.; Wynn, T.; Ding, M.; Borodin, O.; Meng, Y. S.; Xu, K. Bisalt Ether Electrolytes: A Pathway towards Lithium Metal Batteries with Ni-Rich Cathodes. *Energy Environ. Sci.* **2019**, *12*, 780−794.

(20) Sahalie, N. A.; Assegie, A. A.; Su, W.-N.; Wondimkun, Z. T.; Jote, B. A.; Thirumalraj, B.; Huang, C.-J.; Yang, Y.-W.; Hwang, B.-J. Effect of Bifunctional Additive Potassium Nitrate on Performance of Anode Free Lithium Metal Battery in Carbonate Electrolyte. *J. Power Sources* **2019**, *437*, 226912.

(21) Assegie, A. A.; Cheng, J.-H.; Kuo, L.-M.; Su, W.-N.; Hwang, B.-J. Polyethylene Oxide Film Coating Enhances Lithium Cycling Efficiency of an Anode-Free Lithium-Metal Battery. *Nanoscale* **2018**, *10*, 6125−6138.

(22) Assegie, A. A.; Chung, C.-C.; Tsai, M.-C.; Su, W.-N.; Chen, C.-W.; Hwang, B.-J. Multilayer-Graphene-Stabilized Lithium Deposition for Anode-Free Lithium-Metal Batteries. *Nanoscale* **2019**, *11*, 2710−2720.

(23) Wondimkun, Z. T.; Beyene, T. T.; Weret, M. A.; Sahalie, N. A.; Huang, C.-J.; Thirumalraj, B.; Jote, B. A.; Wang, D.; Su, W.-N.; Wang, C.-H.; Brunklaus, G.; Winter, M.; Hwang, B.-J. Binder-Free Ultra-Thin Graphene Oxide as an Artificial Solid Electrolyte Interphase for Anode-Free Rechargeable Lithium Metal Batteries. *J. Power Sources* **2020**, *450*, 227589.

(24) Pande, V.; Viswanathan, V. Computational Screening of Current Collectors for Enabling Anode-Free Lithium Metal Batteries. *ACS Energy Lett.* **2019**, *4*, 2952−2959.

(25) Ishikawa, K.; Harada, S.; Tagawa, M.; Ujihara, T. Effect of Crystal Orientation of Cu Current Collectors on Cycling Stability of Li Metal Anodes. *ACS Appl. Mater. Interfaces* **2020**, *12*, 9341−9346.

(26) Chan, T.-C.; Chueh, Y.-L.; Liao, C.-N. Manipulating the Crystallographic Texture of Nanotwinned Cu Films by Electrodeposition. *Cryst. Growth Des.* **2011**, *11*, 4970−4974.

(27) Zhang, J.; Chen, H.; Fan, B.; Shan, H.; Chen, Q.; Jiang, C.; Hou, G.; Tang, Y. Study on the Relationship between Crystal Plane Orientation and Strength of Electrolytic Copper Foil. *J. Alloys Comp.* **2021**, *884*, 161044.

(28) Lu, L.; Shen, Y.; Chen, X.; Qian, L.; Lu, K. Ultrahigh Strength and High Electrical Conductivity in Copper. *Science* **2004**, *304*, 422.

(29) Lu, L.; Chen, X.; Huang, X.; Lu, K. Revealing the Maximum Strength in Nanotwinned Copper. *Science* **2009**, *323*, 607−610.

(30) Hsiao, H.-Y.; Liu, C.-M.; Lin, H.; Liu, T.-C.; Lu, C.-L.; Huang, Y.-S.; Chen, C.; Tu, K. N. Unidirectional Growth of Microbumps on (111)-Oriented and Nanotwinned Copper. *Science* **2012**, *336*, 1007.

(31) Lu, K. Stabilizing Nanostructures in Metals Using Grain and Twin Boundary Architectures. *Nat. Rev. Mater.* **2016**, *1*, 16019.

(32) Chang, T.; Jin, Y.; Wen, L.; Zhang, C.; Leygraf, C.; Wallinder, I. O.; Zhang, J. Synergistic Effects of Gelatin and Convection on Copper Foil Electrodeposition. *Electrochim. Acta* **2016**, *211*, 245−254.

(33) Lin, C.-C.; Hu, C.-C. The Ultrahigh-Rate Growth of Nanotwinned Copper Induced by Thiol Organic Additives. *J. Electrochem. Soc.* **2020**, *167*, 082505.

(34) Kresse, G.; Furthmüller, J. Efficient iterative schemes forab initiototal-energy calculations using a plane-wave basis set. *Phys. Rev. B* **1996**, *54*, 11169.

(35) Kresse, G.; Joubert, D. From Ultrasoft Pseudopotentials to the Projector Augmented-Wave Method. *Phys. Rev. B* **1999**, *59*, 1758.

(36) Perdew, J. P.; Burke, K.; Ernzerhof, M. Generalized Gradient Approximation Made Simple. *Phys. Rev. Lett.* **1996**, *77*, 3865−3868.

(37) Henkelman, G.; Uberuaga, B. P.; Jónsson, H. A Climbing Image Nudged Elastic Band Method for Finding Saddle Points and Minimum Energy Paths. *J. Chem. Phys.* **2000**, *113*, 9901.

(38) Jónsson, H.; Mills, G.; Jacobsen, K. W. Nudged Elastic Band Method for Finding Minimum Energy Paths of Transitions. *Proc. Int. School Phys.* **1998**, 385−404.

(39) Zhang, X.; Han, J.; Plombon, J.; Sutton, P.; Srolovitz, J.; Boland, J. Nanocrystalline Copper Films Are Never Flat. *Science* **2017**, *357*, 397−400.

(40) Gu, D.; Kim, H.; Lee, J.-H.; Park, S. Surface-Roughened Current Collectors for Anode-Free All-Solid-State Batteries. *J. Energy Chem.* **2022**, *70*, 248−257.

(41) Birhanu, M. K.; Tsai, M.-C.; Kahsay, A. W.; Chen, C.-T.; Zeleke, T. S.; Ibrahim, K. B.; Huang, C.-J.; Su, W.-N.; Hwang, B.-J. Copper and Copper-Based Bimetallic Catalysts for Carbon Dioxide Electroreduction. *Adv. Mater. Interf.* **2018**, *5*, 1800919.

(42) Wood, J. D.; Schmucker, S. W.; Lyons, A. S.; Pop, E.; Lyding, J. W. Effects of Polycrystalline Cu Substrate on Graphene Growth by Chemical Vapor Deposition. *Nano Lett.* **2011**, *11*, 4547−4554.

(43) Yang, Y.; Xiong, J.; Lai, S.; Zhou, R.; Zhao, M.; Geng, H.; Zhang, Y.; Fang, Y.; Li, C.; Zhao, J. Vinyl Ethylene Carbonate as an Effective SEI-Forming Additive in Carbonate-Based Electrolyte for Lithium-Metal Anodes. *ACS Appl. Mater. Interfaces* **2019**, *11*, 6118−6125.

(44) Pei, A.; Zheng, G.; Shi, F.; Li, Y.; Cui, Y. Nanoscale Nucleation and Growth of Electrodeposited Lithium Metal. *Nano Lett.* **2017**, *17*, 1132−1139.

(45) Xu, L.; Dixit, P.; Miao, J.; Pang, J. H. L.; Zhang, X.; Tu, K. N.; Preisser, R. Through-Wafer Electroplated Copper Interconnect with Ultrafine Grains and High Density of Nanotwins. *Appl. Phys. Lett.* **2007**, *90*, 033111.

(46) Liu, W.; Liu, P.; Mitlin, D. Tutorial review on structure - dendrite growth relations in metal battery anode supports. *Chem. Soc. Rev.* **2020**, *49*, 7284−7300.

(47) Biswal, P.; Stalin, S.; Kludze, A.; Choudhury, S.; Archer, L. A. Nucleation and Early Stage Growth of Li Electrodeposits. *Nano Lett.* **2019**, *19*, 8191−8200.

(48) Fang, C.; Li, J.; Zhang, M.; Zhang, Y.; Yang, F.; Lee, J. Z.; Lee, M.-H.; Alvarado, J.; Schroeder, M. A.; Yang, Y.; Lu, B.; Williams, N.; Ceja, M.; Yang, L.; Cai, M.; Gu, J.; Xu, K.; Wang, X.; Meng, Y. S. Quantifying Inactive Lithium in Lithium Metal Batteries. *Nature* **2019**, *572*, 511−515.

(49) Han, J.; Chang, J.; Wei, R.; Ning, X.; Li, J.; Li, Z.; Guo, H.; Yang, Y. Mechanistic Investigation on Tuning the Conductivity Type of Cuprous Oxide (Cu2O) Thin Films via Deposition Potential. *Int. J. Hydrogen Energy* **2018**, *43*, 13764−13777.

(50) Sharova, V.; Moretti, A.; Diemant, T.; Varzi, A.; Behm, R. J.; Passerini, S. Comparative Study of Imide-Based Li Salts as Electrolyte Additives for Li-Ion Batteries. *J. Power Sources* **2018**, *375*, 43−52.

(51) Gong, C.; Pu, S. D.; Gao, X.; Yang, S.; Liu, J.; Ning, Z.; Rees, G. J.; Capone, I.; Pi, L.; Liu, B.; Hartley, G. O.; Fawdon, J.; Luo, J.; Pasta, M.; Grovenor, C. R. M.; Bruce, P. G.; Robertson, A. W. Revealing the Role of Fluoride-Rich Battery Electrode Interphases by Operando Transmission Electron Microscopy. *Adv. Energy Mater.* **2021**, *11*, 2003118.